View Article Online
View Journal

Dalton Transactions

An international journal of inorganic chemistry

Accepted Manuscript

This article can be cited before page numbers have been issued, to do this please use: C. Chuang, C. Hsueh, K. Wu, C. Shen, T. Lin and C. Kung, *Dalton Trans.*, 2026, DOI: 10.1039/D5DT02918J.

ROYAL SOCIETY OF CHEMISTRY

rsc.li/dalton

View Article Online
DOI: 10.1039/D5DT02918J

ARTICLE

Two-dimensional metal–organic framework/graphene oxide composites as proton conductors: Chemical grafting *vs.* physical blending

Received 00th January 20xx,
Accepted 00th January 20xx

DOI: 10.1039/x0xx00000x

Chi-Lun Chuang,[a] Chou-Hung Hsueh,[a] Kuan-Chu Wu,[a] Cheng-Hui Shen,[a] Tzu-Chi Lin [a] and Chung-Wei Kung *[abc]

A water-stable two-dimensional (2D) zirconium-based metal–organic framework (MOF), ZrBTB (BTB = 1,3,5-tri(4-carboxyphenyl)benzene), serves as a porous platform to integrate with graphene oxide (GO) in order to achieve ultrahigh proton conductivity (σ). Two synthetic methods, chemical grafting and physical blending, are used for preparing various nanocomposites composed of ZrBTB and GO. Porosity, morphology and proton-conducting characteristics of these composites and both pristine materials are investigated. The nanocomposite obtained by the grafting method with a GO loading of around 1 wt%, ZrBTB–0.01GO, possesses coordination bonds between GO and the hexa-zirocnium nodes of ZrBTB; such chemical grafting reduces the number of accessible –OH/–OH_2 pairs on the MOF nodes. ZrBTB–0.01GO thus exhibits a worse proton-conducting performance, with a σ of 3.93 × 10^{-3} S cm^{-1} at 60 °C and 99% relative humidity (RH), compared to those of the pristine ZrBTB (1.57 × 10^{-2} S cm^{-1}) and pristine GO (8.68 × 10^{-3} S cm^{-1}), respectively. In contrast, considerably increased proton conductivities and decreased activation energies are achieved with the same GO loading by the physical blending method, with ZrBTB/0.01GO exhibiting a σ of 4.01 × 10^{-2} S cm^{-1} at 60 °C and 99% RH and an activation energy of 0.28 eV. At an optimal GO loading, the resulting 2D nanocomposite, ZrBTB/0.005GO, can achieve an ultrahigh σ of 1.03 × 10^{-1} S cm^{-1} at 60 °C under 99% RH with a small activation energy of 0.18 eV. Findings here suggest that compared to the commonly reported chemical grafting method, the physical blending method is more advantageous for preparing proton-conductive 2D MOF-based nanocomposites with more accessible proton-relaying functional groups and thus better performance.

Introduction

Metal–organic frameworks (MOFs), as a class of highly ordered and designable porous materials, have undergone rapid development since the early 21st century.[1, 2] They have been extensively applied in various fields, including gas adsorption and storage,[3, 4] separation,[5, 6] catalysis,[7, 8] sensing,[4, 9, 10] and energy storage.[11, 12] In addition to the aforementioned applications, benefiting from their high porosity, structural tunability to incorporate hydrophilic functional groups, and insulating nature for electrons, MOFs have also attracted great attention as promising proton-conductive materials.[13-20] On the other hand, acidic water electrolysers are crucial devices to produce green hydrogen, and proton exchange membrane fuel cells (PEMFCs) are known as one of the most promising energy-conversion technologies for hydrogen utilisation.[21] In both systems, the proton exchange membrane (PEM) capable of conducting protons in acidic aqueous environments plays a crucial role in determining the overall performance.[22] Consequently, stable MOFs with superior proton-conducting characteristics are highly attractive materials for energy-related applications, including fuel cells and PEM electrolysers.

It is well known that most MOFs exhibit poor chemical stability in aqueous media.[23] Recent developments in chemically robust tetravalent MOFs, including titanium-, zirconium-, cerium(IV)-, and hafnium-based frameworks, have opened new possibilities for utilising MOFs in humid or aqueous environments.[23-26] Hence, these stable MOFs have been widely investigated as proton conductors, with most studies focusing on three-dimensional (3D) MOFs to date.[15, 27-29] Compared to 3D MOFs, two-dimensional (2D) MOFs with crystallographically well-defined 2D structures are supposed to offer shorter hopping distances for ionic species to move between stacked molecular sheets. However, studies reporting proton conduction in 2D tetravalent MOFs are still very rare.[30-33] Recently, Wang and co-workers reported the first study on proton-conducting characteristics of ZrBTB (BTB = 1,3,5-tri(4-carboxyphenyl)benzene), a six-connected 2D

[a] Department of Chemical Engineering, National Cheng Kung University, Tainan City, 70101, Taiwan.
[b] Program on Key Materials, Academy of Innovative Semiconductor and Sustainable Manufacturing, National Cheng Kung University, Tainan City, 70101, Taiwan.
[c] Center for Resilience and Intelligence on Sustainable Energy Research (RiSER), National Cheng Kung University, Tainan City, 70101, Taiwan.
* Corresponding author: cwkung@mail.ncku.edu.tw (C.-W. K.)
Electronic Supplementary Information (ESI) available: [Additional experimental data]. See DOI: 10.1039/x0xx00000x

View Article Online
DOI: 10.1039/D5DT02081J

zirconium-based MOF, and its proton conductivity (σ) was found to be much higher than those of several pristine 3D tetravalent MOFs.[33] We thus reasoned that stable 2D MOFs, such as ZrBTB, should be promising candidates for designing high-performance proton conductors.

To further enhance the σ of the pristine MOF, several strategies have been widely employed, such as the introduction of hydrophilic/proton-relaying functional groups and the incorporation of proton-conductive guest molecules in MOFs.[16, 33-35] One of the effective approaches is the integration of the porous MOF with another proton-conductive material, such as graphene oxide (GO), to form nanocomposites with heterostructural interfaces.[36-38] GO with a high degree of oxidation is electrically insulating, and it possesses abundant oxygen-containing functional groups to, not only facilitate the adsorption of water molecules, but also extend the proton-transport pathways.[39] MOF-GO composites have thus been reported as better proton conductors than both pristine materials. For example, ZIF-8@GO,[36] GO@UiO-66-NH_2[37] and MIL-101/GO[38] were reported as excellent proton conductors with a Grotthuss-type mechanism.[40, 41] But it should be noticed that, all aforementioned studies investigating proton conduction in MOF-GO composites utilised 3D MOFs grown or grafted on GO, with chemical bonds formed between MOF crystals and GO layers. The resulting σ could usually be enhanced owing to the exfoliation of GO layers caused by the bulky MOF crystals presented in between. In contrast, the physical blending of MOF crystals and GO was usually employed as a referencing method.[36, 38] However, it is worth mentioning that the chemical grafting or growing of MOF crystals onto GO sheets should also reduce the accessible hydrophilic groups exposed on the external surface of both materials, which is not desirable for proton conduction. This effect may be more significant when small MOF crystals or even 2D MOF nanosheets are used. Effects of synthetic approaches for MOF-GO composites on the resulting proton-conducting performance have barely been explored.

In this study, a chemically robust 2D MOF, ZrBTB,[42-44] was employed as a platform for the integration with GO. As the first study reporting composites with a 2D MOF and GO as proton conductors, two synthetic methods, including the chemical grafting (ZrBTB–GO) and the physical blending (ZrBTB/GO), were employed; see Figure 1. With the use of physical blending, we aim to develop a new type of 2D MOF-based nanocomposite with an ultrahigh σ, featuring both shorter pathways for proton transport and a high density of protonic carriers. Results suggest that the optimised nanocomposite, ZrBTB/0.005GO, can achieve an ultrahigh σ of 1.03×10^{-1} S cm^{-1} at 60 °C under 99% relative humidity (RH) with a comparatively small activation energy (E_a) of 0.18 eV, which is significantly better than both the pristine materials and the chemically grafted composite.

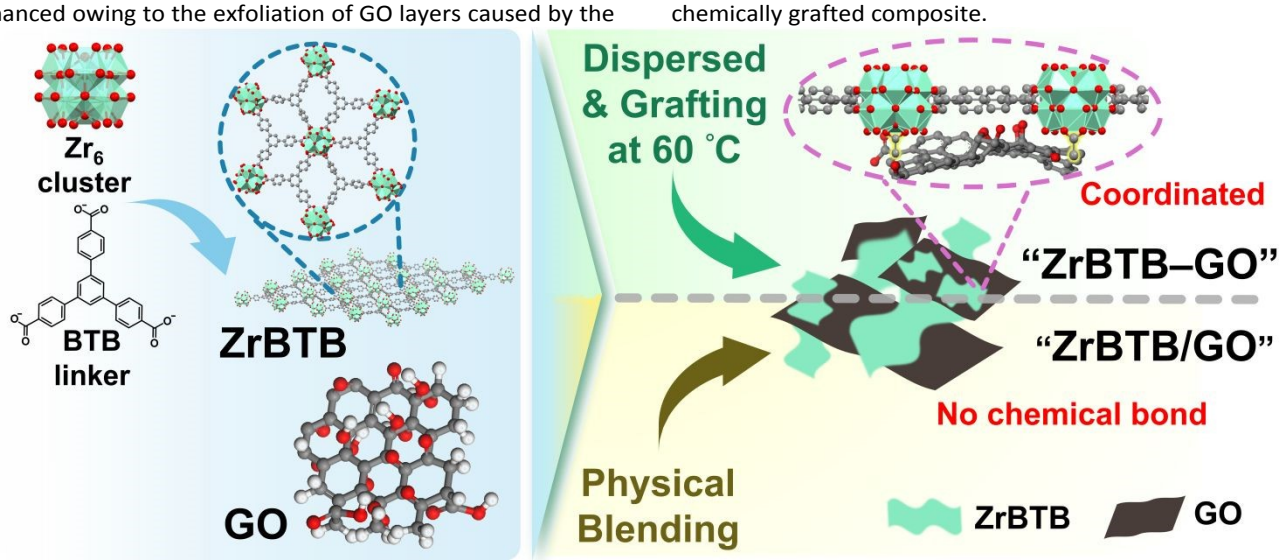

Figure 1. Schematic diagram for the synthesis of MOF-GO nanocomposites by chemical grafting or physical blending.

Experimental

1. Chemicals

Zirconium(IV) chloride ($ZrCl_4$, 98%), potassium nitrate (KNO_3, 99%) and 1,3,5-tri(4-carboxyphenyl)benzene (H_3BTB, 97%) were obtained from Thermo Fisher Scientific. Benzoic acid (BA, 99.5%), potassium carbonate (K_2CO_3, 98%), sodium bromide (NaBr, 98%), sodium chloride (NaCl, 99%) and deuterium oxide (D_2O, 99.9 atom% D) were purchased from Sigma-Aldrich. N,N-dimethylformamide (DMF, ≥99.8%), dimethyl sulfoxide (DMSO, 99%) and potassium chloride (KCl, 99.0%) were obtained from Duksan Pure Chemicals. Hydrochloric acid (HCl, 36.5–38.0%) was received from J.T. Baker. Potassium bromide (KBr, ≥99.0%) was purchased from Honeywell Fluka. Acetone (≥99%) and ethanol (95%) were obtained from Uni-Onward Co., Ltd., Taiwan. Graphene oxide (GO, model number: EW-GO1, 97%, oxygen content=45%) powder was purchased from E-WAY Technology Co., Ltd., Taiwan. All the chemicals mentioned above were used as received without purification. Deionised water was used throughout the entire work.

2. Synthesis of materials

The synthesis of ZrBTB was performed according to the procedure in our recent work.[45, 46] First, $ZrCl_4$ (100 mg), H_3BTB (100 mg), and BA (6 g) were dissolved in a mixture of DMF (30

View Article Online
DOI: 10.1039/D5DT02818J

mL) and water (30 mL) using ultrasonication. The resulting solution was then transferred into a DURAN® 100-mL glass laboratory bottle. The homogeneous mixture was placed in a colourless bottle, sealed with a polytetrafluoroethylene (PTFE)-lined polybutylene terephthalate cap, and the bottle was then placed in an oven at 120 °C for 48 h. After the MOF growth, the mixture was cooled to room temperature (RT) and centrifuged at 5000 rpm to remove the supernatant. The centrifugation was performed three times, after adding 30 mL of fresh DMF every time, to effectively remove excess reagents. Afterwards, the powder was subjected to centrifugal washing with acetone (30 mL) three times to ensure the complete solvent exchange, with the immersion periods of 2 h, overnight and 2 h between each step. The powder was then activated in a vacuum oven at 60 °C overnight. Subsequently, to effectively remove the coordinated benzoate, 100 mg of the activated MOF powder was dispersed in a prepared solution containing DMSO (30 mL), water (0.4 mL) and 12 M HCl (0.8 mL) through ultrasonication, and the mixture was kept at RT for 18 h. Then, the solid was washed with DMSO (30 mL) four times over 8 h, followed by the solvent exchange with acetone three times. The "ZrBTB" powder was finally obtained after activation in a vacuum oven at 60 °C overnight.

For the synthesis of MOF/GO nanocomposites through physical blending, 10 mg of GO was first dispersed in 10 mL of ethanol by ultrasonication for 1 h. Thereafter, a certain amount of GO-containing suspension was added into an agate mortar, followed by the evaporation of solvent at RT. Thereafter, 100 mg of ZrBTB was added, and the mixture was ground for 3 min. The obtained materials prepared with 0.1, 0.5, 1.0 and 3.0 mL of the GO suspension were named as "ZrBTB/0.001GO," "ZrBTB/0.005GO," "ZrBTB/0.01GO" and "ZrBTB/0.03GO," respectively.

To perform the chemical grafting between ZrBTB and GO, the following procedure from a reported study was used.[47] GO (10 mg) was dispersed in ethanol (10 mL) by ultrasonication for 1 h, and ZrBTB (100 mg) powder was dispersed in ethanol (4 mL) to form another suspension. Then, the GO-containing suspension (1 mL) was added into the ZrBTB-based suspension in a 20-mL scintillation vial, and the mixture was ultrasonicated for 10 min. Thereafter, the vial was sealed with a PTFE-lined cap and heated in an oil bath at 60 °C for 24 h under stirring at 200 rpm. After the reaction, the obtained solid was washed with ethanol (10 mL) three times through centrifugation, and the solvent exchange was performed with acetone (10 mL) three times. The obtained material was then dried in a vacuum oven at 60 °C overnight, and it was designated as "ZrBTB–0.01GO."

3. Preparation of pellets for measuring conductivities

The procedure for preparing pellets was slightly modified from that in our recently published work.[29] First, to allow a fair comparison with MOF/GO nanocomposites prepared by physical blending, powders of ZrBTB, GO and ZrBTB–0.01GO were ground for 3 min in an agate mortar before the pelletisation. Thereafter, approximately 15 mg of the sample powder was filled into a die set (d = 7 mm) equipped with a mini-pellet press (Specac), and the pelletising process was performed with a load of 0.3 tons for 3 seconds. This process was repeated three times to form a stable pellet. The thickness of each pellet was measured by a digital calliper (Mitutoyo). The resulting pellet was then sandwiched between two titanium plates and dried in a vacuum oven at 60 °C overnight before any measurement.

4. Measurements of proton and electrical conductivities

The entire procedure was slightly modified from that reported in our previous work.[29] For measuring its proton conductivity, the sandwiched pellet was first placed in the headspace of a hermetically sealed glass chamber loaded with water, with two wires connecting to both sides of the pellet. The chamber was then located in an oven at 30 °C for 48 h to reach 99% RH. Thereafter, electrochemical impedance spectroscopy (EIS) of the pellet was measured using a PGSTAT204 potentiostat/galvanostat (Autolab, Eco-Chemie, The Netherlands) equipped with a FRA2 module under a two-electrode mode. Each EIS measurement was performed at an applied voltage of 0 V, with an amplitude of 10 mV and a frequency range from 1 MHz to 1 Hz. The proton conductivity of the pellet at each temperature was measured every 5 °C from 30 °C to 60 °C. At each temperature, EIS measurement was performed 30 min after the chamber had stabilised at the targeted temperature. The measurement of each material was performed three times. The same process was employed to measure proton conductivities of the pellet in D_2O vapour, except that water was replaced by D_2O.

For measuring the proton conductivities under various levels of RH, the chamber was set at 30 °C, and the same process mentioned above was used except for replacing water with the saturated aqueous solution of K_2CO_3, NaBr, NaCl, KCl, or KNO_3 loaded in the sealed glass chamber; it could thus achieve the RH of 45, 58, 75, 84 or 94% in the headspace, respectively, measured by a humidity sensor (GM1361, Benetech).

For measurements of electrical conductivity, the sandwiched pellet was connected to the CHI6273E electrochemical workstation (CH Instruments Inc.) to perform current–voltage (*I*–*V*) measurements with a two-electrode setup.[29] The *I*–*V* curve of each pellet was collected at RT in air.

5. Instrumentations

X-ray diffraction (XRD) patterns of samples were measured using a SmartLab (Rigaku) with CuKα radiation (λ = 0.15406 nm). Nitrogen adsorption-desorption isotherms were collected at 77 K using a 3FLEX (Micromeritics) after degassing the powder samples overnight at 110 °C with a VacPrep (Micromeritics). Scanning electron microscopic (SEM) images were collected using a SU-8230 (Hitachi) at an operative voltage of 10 kV. A JEM-1400 Flash (JEOL) was used to collect transmission electron microscopic (TEM) images and energy-dispersive X-ray spectroscopic (EDS) data under an operative voltage of 120 kV. Fourier transform infrared (FTIR) measurements were performed on a Nicolet 6700 (Thermo Fisher Scientific). For preparing FTIR samples, the material for testing was ground with KBr followed by the pelletising

View Article Online
DOI: 10.1039/D5DT02916T

process to get a pellet. TGA experiments of the samples were conducted on a thermal analyser (Setaram Labsys evo) in a nitrogen flow. For preparing TGA samples, the solid material was placed in a hermetically sealed chamber at 30 °C and 99% RH for 48 h, followed by the TGA measurement immediately. X-ray photoelectron spectroscopy (XPS) spectra were collected using a Theta Probe angle-resolved XPS spectrometer (Thermo Fisher Scientific). All spectra were corrected by referencing the strongest C 1s peak originating from C–C bonds to 284.8 eV before analysing the data. During the synthesis of ZrBTB and its composites, a Heraeus Megafuge 16 centrifuge with a TX-400 rotor (Thermo Fisher Scientific) was utilised for the centrifugation during all washing and solvent-exchange steps.

Results and Discussion

1. Materials characterisations

ZrBTB was synthesised by a solvothermal method using BA as the modulator during crystal growth, followed by the treatment with hydrochloric acid to replace the capping benzoate with terminal –OH/–OH_2 ligands on its hexa-zirconium nodes.[45] Nanocomposites composed of ZrBTB and the commercially available GO were then prepared by two synthetic methods. Crystallinities of all materials were first verified through powder XRD. As shown in Figure 2(a) and Figure S1, XRD patterns of ZrBTB and all composites are consistent with the simulated pattern of ZrBTB, with main diffraction peaks located at 5.2°, 9.0° and 10.4°, which correspond to the planes of 100, 110 and 200, respectively.[42, 45, 46, 48] This finding suggests that the crystalline structure of ZrBTB was successfully formed during the MOF growth, and its crystallinity can be well preserved after the integration with GO. In addition, the strong diffraction peak in the experimental XRD pattern of GO located at 11.1°, attributed to the interlayer distance between stacked graphene sheets,[49] is not observable in the patterns of all composites. Even in the pattern of ZrBTB/0.03GO with a relatively high GO loading of almost 3 wt%, this diffraction peak from stacked GO is still not observed (see Figure S1). This absence indicates that in each nanocomposite, the stacked GO layers become mostly separated into small grains with poor long-range order; it thus confirms the successful formation of uniform composites with ZrBTB sheets and less stacked GO layers.

Nitrogen gas (N_2) adsorption-desorption measurements were performed at 77 K to examine the porosity of each material. The obtained isotherms and specific surface areas calculated based on the Brunauer–Emmett–Teller (BET) method are shown in Figure 2(b) and Figure S2(a). All isotherms of ZrBTB and MOF-based nanocomposites exhibit a steep gas uptake at low relative pressures and a hysteresis loop in the high-pressure region, corresponding to the microporosity of the stacked 2D sheets of ZrBTB and the mesoporous cavity between large aggregates of MOF sheets, respectively.[50] Furthermore, the BET surface area of ZrBTB was estimated as 316 m^2 g^{-1}. All these characteristics are consistent with those reported for ZrBTB.[48, 50] In contrast, as revealed in Figure 2(b), the GO shows negligible nitrogen uptake at 77 K. After integrating ZrBTB with GO, the BET surface area of each composite becomes slightly smaller than that of the pristine ZrBTB, but all composites still possess BET surface areas larger than 230 $m^2 g^{-1}$. It indicates that the major porosity of ZrBTB is still preserved in every nanocomposite. Pore size distributions of MOF-based materials were also extracted from their isotherms by using the model of density functional theory (DFT) for carbon-slit pores. As revealed in Figure S2(b), ZrBTB and all nanocomposites possess two kinds of main pore sizes located at around 0.7-0.8 nm and 1.2-1.3 nm, which originate from the interlayer space between stacked molecular sheets of ZrBTB and the aperture on the 2D sheet of ZrBTB, respectively.[45, 48, 50]

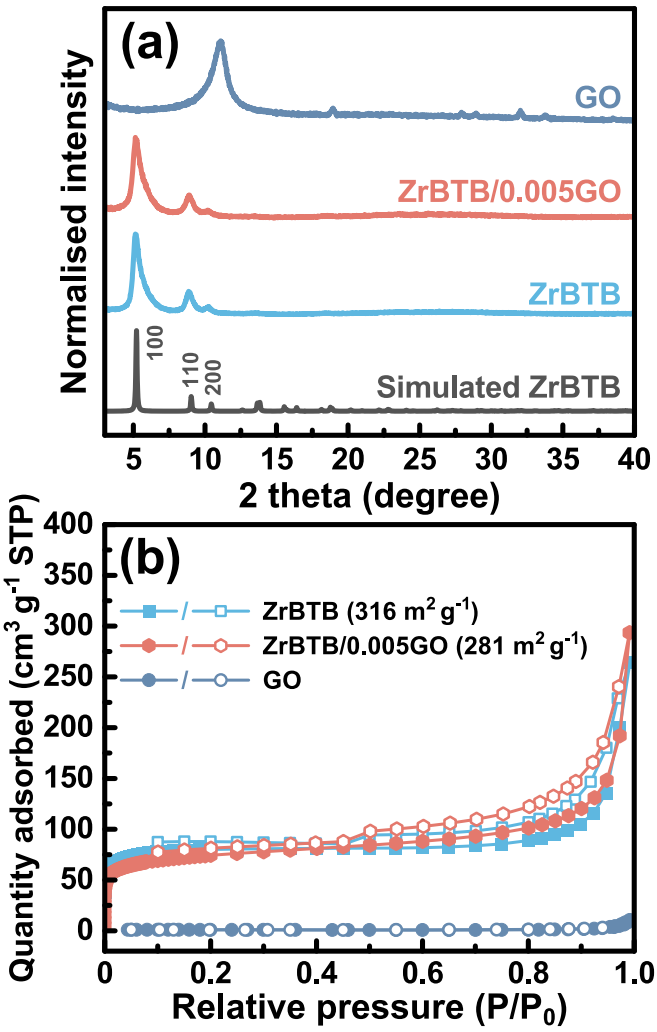

Figure 2. (a) Powder XRD patterns and (b) N_2 adsorption-desorption isotherms of ZrBTB, GO and ZrBTB/0.005GO. The simulated pattern of ZrBTB is also shown in (a) and BET specific surface areas are provided in (b). Solid and empty scatters in (b) indicate data for adsorption and desorption, respectively.

SEM and TEM images of ZrBTB, GO and three representative nanocomposites were collected in order to probe their morphologies, and the results are shown in Figure 3. For ZrBTB, as revealed in Figure 3(a), it is composed of loosely stacked 2D sheets with a flower-like morphology, and the similar morphology can also be observed in its TEM image (Figure 3(f)). This morphology is consistent with that reported for ZrBTB in previous studies.[46, 51] On the other hand, GO

exhibits a morphology of aggregates in its SEM image (Figure 3(b)), but exfoliated GO sheets can be found in its TEM image (Figure 3(g)). For all the three nanocomposites including ZrBTB–0.01GO, ZrBTB/0.01GO and ZrBTB/0.005GO, the similar flower-like morphology of 2D MOF can be observed in their SEM images. However, as shown in Figure 3(c-e), tiny particles randomly attaching onto the flower-like MOF sheets can be found. Such morphologies become more obvious in TEM images of these nanocomposites (Figure 3(h-j)), revealing that these materials are composed of aggregates of loosely packed tiny 2D sheets. Findings here indicate that the incorporation of a small amount of GO into ZrBTB, either by chemical grafting or physical blending, can result in a significant morphological change from both pristine materials, but the 2D characteristic morphology can still be observed in all nanocomposites. The representative nanocomposite, ZrBTB/0.005GO, was then subjected to EDS measurements, and the results are shown in Figure S3. The elemental mapping data in Figure S3(d) indicate that all elements, including zirconium, carbon and oxygen, are uniformly located on those loosely packed 2D sheets in the nanocomposite.

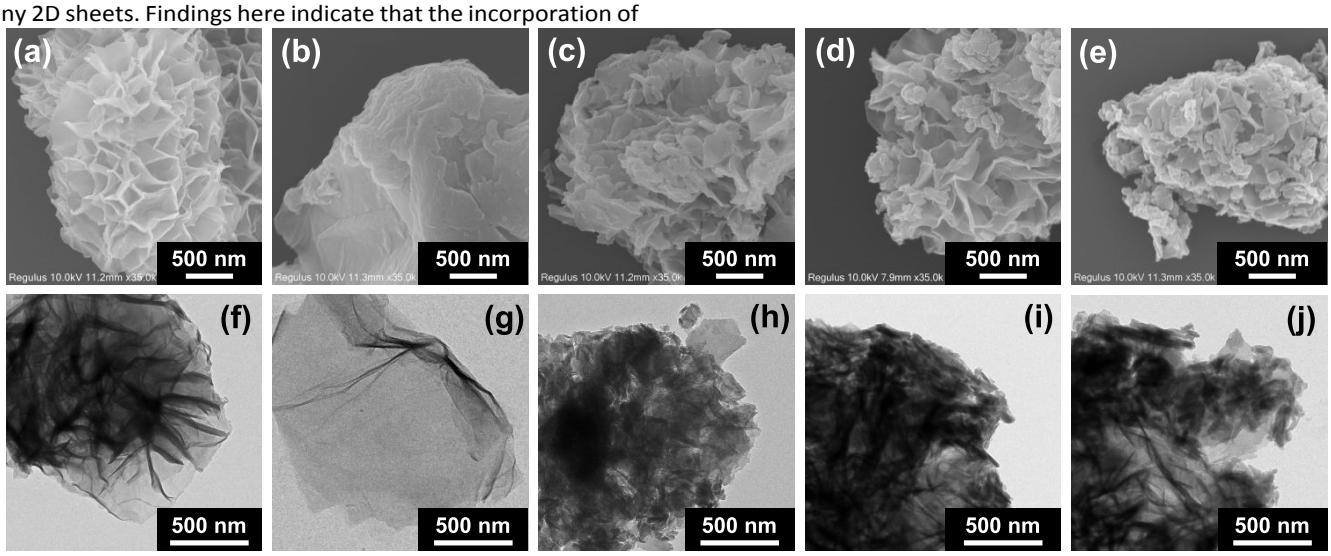

Figure 3. SEM and TEM images of (a, f) ZrBTB, (b, g) GO, (c, h) ZrBTB–0.01GO, (d, i) ZrBTB/0.01GO and (e, j) ZrBTB/0.005GO.

To probe the interaction between ZrBTB and GO in the composites synthesised by various methods, FTIR spectra of all materials were collected with the use of their pellets ground with KBr. The obtained data are shown in Figure S4, and the normalised spectra are plotted in Figure 4. Characteristic peaks of ZrBTB located at 1416 and 1544 cm^{-1} are associated with the symmetric and asymmetric stretching vibrations of coordinated bidentate carboxylate groups, respectively.[52] Other key peaks at 1589 and 1605 cm^{-1}, though not clearly defined in the literature, could be attributed to the C=C stretching vibrations of the aromatic ring in the BTB linker,[45, 48] or the C=O vibrations of coordinated unidentate carboxylate groups.[53] These characteristic peaks can be observed in all MOF-based materials. This result indicates that the coordination between linkers and hexa-zirconium nodes in the 2D MOF is well preserved in all composites. FTIR spectrum of the pristine GO also displays several characteristic peaks, including the C=O stretching vibration of the carboxyl group at 1718 cm^{-1}, O–H bending vibration of the adsorbed water at 1620 cm^{-1}, O–H bending vibration at 1373 cm^{-1}, C–O stretching vibration of the epoxy group at 1196 cm^{-1}, and C–O stretching vibration of alkoxy groups at 1101 and 1047 cm^{-1}, respectively; these features agree well with those of GO with a high degree of oxidation reported in previous studies.[54-56] After integrating GO into ZrBTB, a small peak of C=O stretching from the free carboxylic group of GO, located at approximately 1700 cm^{-1}, can be observed in the FTIR spectra of all nanocomposites. It is worth noticing that a new peak at 1654 cm^{-1} can be clearly observed, exclusively in the FTIR spectrum of ZrBTB–0.01GO, which should be associated with the C=O/C–O vibrational features from the direct coordination of carboxylate group in the GO onto the hexa-zirconium node of ZrBTB to form C–O–Zr bonds.[38] The finding here clearly indicates that, although the ZrBTB–0.01GO and ZrBTB/0.01GO show almost the same crystallinity, porosity and morphology as discussed previously, they do possess quite different interactions between GO and MOF. After the chemical grafting between co-dispersed GO and ZrBTB sheets at 60 °C, significant coordination bonds between GO and MOF are presented in the resulting ZrBTB–0.01GO.

View Article Online
DOI: 10.1039/D5DT01981

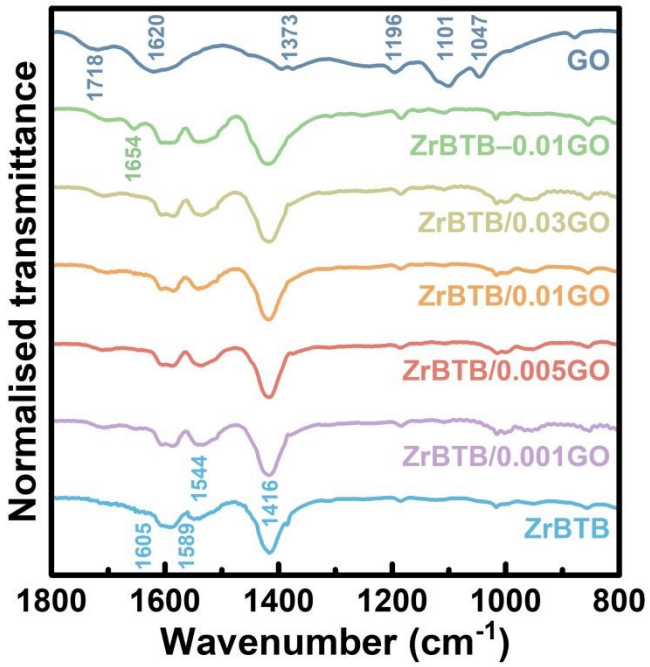

Figure 4. FTIR spectra of ZrBTB, GO and all nanocomposites. Characteristic peaks are listed.

XPS measurements were performed to further characterise ZrBTB, GO, ZrBTB–0.01GO and ZrBTB/0.01GO. From the survey spectra in Figure S5, signals of corresponding elements in each material can be detected. High-resolution XPS spectra were then collected in C 1s, O 1s and Zr 3d regions, and the obtained results are shown in Figures S6, S7 and S8, respectively. Peaks in the region of C 1s were deconvoluted and identified according to a previous study.[57] On the other hand, characteristic peaks of Zr-MOF and GO in the region of O 1s were identified by following previous studies.[57-60] As shown in Figures S6 and S7, for both C 1s and O 1s regions, peaks of corresponding functional groups in ZrBTB and GO can be found in their corresponding spectra, respectively. Peaks from both pristine materials are also in general observable in spectra of both composites in Figures S6 and S7. In addition, an obvious difference can be observed in XPS spectra collected in the region of Zr 3d. As shown in Figure S8, the physically blended composite, ZrBTB/0.01GO, shows almost the same XPS spectrum as the pristine ZrBTB, while the spectrum of ZrBTB–0.01GO reveals a positive shift of 0.4 eV in its Zr 3d peaks. Such a peak shift should be attributed to the change in coordination environments on the hexa-zirconium nodes of MOF, rendering zirconium atoms more electron-deficient.[61, 62] Agreeing with the FTIR observation, XPS result here clearly indicates the coordination of GO onto the hexa-zirconium nodes of ZrBTB in the composite synthesised by chemical grafting.

2. Proton conductivity of ZrBTB, GO and nanocomposites

Since proton conductors usually require an electrically insulating feature, the electrical conductivities of ZrBTB, GO, and three representative nanocomposites were first quantified by measuring *I–V* curves of their pellets. Detailed protocols for such a two-probe *I–V* method can be found in our previous work.[29, 50] *I–V* data are plotted in Figure S9, and the calculated values of electrical conductivity are listed in Table S1. ZrBTB and GO possess electrical conductivities of 3.46×10^{-12} S cm^{-1} and 7.93×10^{-9} S cm^{-1}, respectively, suggesting that both pristine materials are electrical insulators. For all nanocomposites tested here, their electrical conductivities are in the range of 10^{-11} S cm^{-1}, which are around two orders of magnitude lower compared to that of GO.

Proton-conducting performances of all materials were then evaluated by performing EIS measurements. The σ of each material was measured at various temperatures (T) using EIS spectra and calculated according to the method described in Section 1 of ESI. The resulting Nyquist plots of the ZrBTB, GO, ZrBTB–0.01GO and ZrBTB/0.01GO are shown in Figure S10, and the obtained σ values are plotted in Figure 5(a). At 60 °C and 99% RH, proton conductivities of the pristine ZrBTB and GO are 1.57×10^{-2} S cm^{-1} and 8.68×10^{-3} S cm^{-1}, respectively, which are consistent with the values reported in previous studies.[33, 39] After the integration of both materials by the grafting method, ZrBTB–0.01GO exhibits a σ of 3.93×10^{-3} S cm^{-1} at 60 °C and 99% RH, which is inferior to both pristine materials. In contrast, ZrBTB/0.01GO, the composite prepared by physical blending, achieves a high σ of 4.01×10^{-2} S cm^{-1}, which is about 2.5-fold higher than that of the pristine ZrBTB and 4.6-fold higher than that of the pristine GO. The E_a for proton conduction in each material was subsequently calculated from the linear fitting of Arrhenius plots; see detailed protocols in Section 1 of ESI. Results for the above materials are shown in Figure 5(b). The pristine materials, ZrBTB and GO, exhibit E_a values of 0.28 eV and 0.32 eV, respectively, which are consistent with previously reported values.[33, 39] For the composites, ZrBTB–0.01GO exhibits an E_a of 0.35 eV, which is larger than those of both pristine materials. In contrast, ZrBTB/0.01GO shows an E_a of 0.28 eV, the same as that of the pristine ZrBTB. Findings here clearly indicate that with around 1 wt% of GO in the 2D MOF-GO nanocomposite, the physically blended material can outperform both pristine materials for proton conduction, while the chemically grafted composite shows the worst proton-conducting performance compared to others.

View Article Online
DOI: 10.1039/D5DT02918J

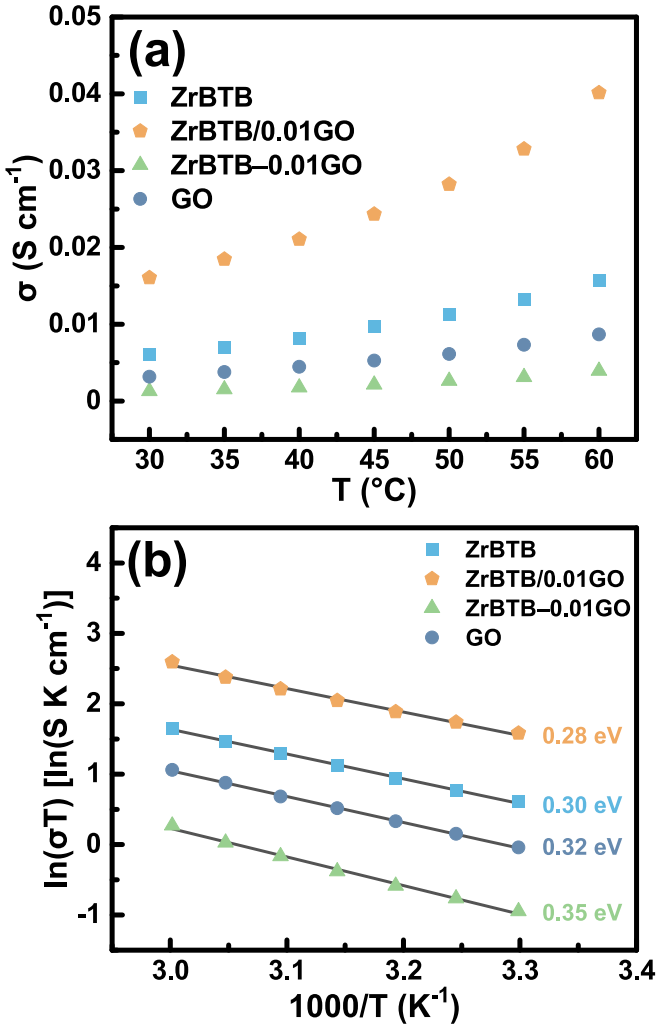

Figure 5. (a) Proton conductivity at each temperature and 99% RH, and (b) Arrhenius plot obtained from proton conductivities of ZrBTB, GO, ZrBTB–0.01GO and ZrBTB/0.01GO. Activation energies are listed in (b).

Since E_a values of ZrBTB, GO and the two nanocomposites are all below 0.4 eV, such results suggest that the proton transport within these materials predominantly proceeds *via* the Grotthuss mechanism. However, the ZrBTB–0.01GO, in terms of both σ and E_a, exhibits the worst performance compared to both pristine materials, which is unexpected compared to the findings of several previously reported chemically grafted MOF-GO composites with 3D MOFs.[36-38] One plausible reason is that the pristine ZrBTB already exhibits a higher proton conductivity than GO. Therefore, the prevention of GO from stacking through the coordination-driven grafting of ZrBTB sheets is insufficient to further enhance the proton conductivity. Furthermore, the coordination of ZrBTB and GO through carboxylate groups, as evidenced by the FTIR spectrum, should largely reduce the numbers of accessible proton-relaying groups in both materials and thus disrupt the hydrogen-bonding network essential for proton transport. Such effects thus result in a decrease in σ and an increase in E_a after chemically grafting the 2D MOF and GO together. Results here suggest that for synthesising proton-conductive nanocomposites with 2D MOF and GO, the physical blending method, which does not generate coordination bonds between both materials, should be more advantageous compared to the chemical grafting method that is typically used for 3D MOFs.

To clarify the effect of GO loading on the proton-conducting performance of the resulting material, a series of composites with varying GO loadings were prepared by physical blending for measuring their proton conductivities. Nyquist plots are shown in Figure S11, and the results are summarised in Figure 6(a-b). It can be found that all physically blended composites tested here exhibit larger values of σ compared to both pristine materials, and the ZrBTB/0.005GO shows the optimal performance among all materials. An ultrahigh σ of 1.03×10^{-1} S cm^{-1} and a low E_a of 0.18 eV can be achieved at 60 °C and 99% RH, outperforming many of those highly proton-conductive MOF-based and GO-based materials reported previously (Table S2).

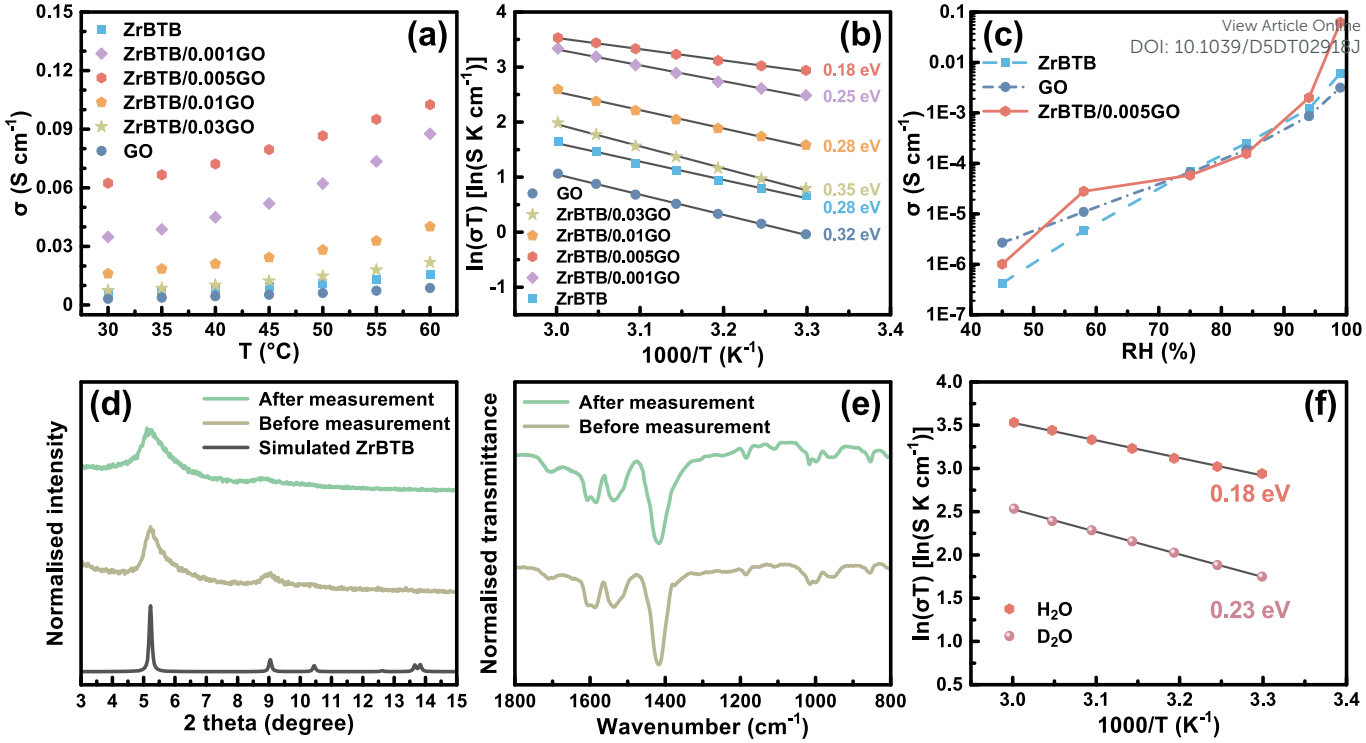

Figure 6. (a) Proton conductivities of ZrBTB, GO and various physically blended nanocomposites, measured at different temperatures and 99% RH, and (b) the corresponding Arrhenius plot from (a). (c) Proton conductivities of ZrBTB, GO and ZrBTB/0.005GO, measured under various RH levels at 30 °C. (d) Grazing incidence XRD patterns and (e) FTIR spectra of ZrBTB/0.005GO pellets, measured before and after the proton conductivity measurements under 99% RH at various temperatures from 30 °C to 60 °C. (f) Arrhenius plot of ZrBTB/0.005GO measured under the atmospheres of H_2O and D_2O vapours, respectively. Activation energies are listed in (b) and (f), and the simulated XRD pattern of ZrBTB is provided in (d) for comparison.

Since RH strongly influences the proton conduction in MOF-based materials, varying RH levels is an effective approach to investigate the underlying conducting mechanism. Proton conductivities of ZrBTB/0.005GO and both pristine materials were measured at 30 °C under 94, 84, 75, 58 and 45% RH, respectively, and the obtained Nyquist plots are shown in Figure S12. As illustrated in Figure 6(c), σ values of both ZrBTB and GO increase gradually from around 10^{-6} S cm^{-1} to 10^{-3} S cm^{-1} when RH rises from 45% to 99%. ZrBTB/0.005GO exhibits a similar trend in σ to both pristine materials in the region below 84% RH. However, its σ increases sharply and becomes outperforming compared to both pristine materials, only when the RH increases from 84% to 99%. This observation indicates that ZrBTB/0.005GO requires a sufficient water uptake to achieve higher σ compared to both pristine materials, exhibiting an ultrahigh conductivity under the RH of 94% or that approaching saturation. In addition, ZrBTB/0.005GO can preserve its crystallinity and coordinating characteristics after both the pelletisation and EIS measurements under 99% RH, as evidenced by both the grazing incidence X-ray diffraction (GIXRD) patterns and FTIR spectra shown in Figure 6(d) and Figure 6(e).

To probe the kinetic isotope effect of water vapour and verify that proton is the species being transported within these materials, σ values at various temperatures were measured in the presence of D_2O vapour for ZrBTB/0.005GO and both pristine materials. The resulting Nyquist plots are shown in Figure S13, and the corresponding Arrhenius plots are shown in Figure 6(f) and Figure S14. σ values of the ZrBTB and GO in the presence of D_2O vapour are reduced by factors of 1.6 and 1.4, respectively, compared to those measured under H_2O vapour over the entire temperature range. Results here are consistent with the theoretical expectation that σ values should be inversely proportional to the square root of the atomic mass of protonic carriers.[29] Notably, the difference in σ observed for ZrBTB/0.005GO under H_2O and D_2O is around 3-fold, substantially greater than those for both pristine materials. Such an enhanced sensitivity to the isotopic substitution indicates the presence of augmented proton-hopping transport strongly relying on the hydrogen-bonding network and hydrophilic functional groups,[33, 63] as observed in other proton-conductive materials as well.[33, 64, 65]

3. Water uptakes in ZrBTB, GO and nanocomposites

Results discussed previously indicate that 2D ZrBTB-GO nanocomposites prepared by chemical grafting and physical blending can achieve quite different proton-conducting characteristics, and the physically blended composite can exhibit significantly higher σ than both pristine materials when the RH in the testing environment is close to saturation. We thus hypothesised that such differences in proton-conducting behaviours should be attributed to the affinity between the material and water molecules coming from the external environment. To test this hypothesis, ZrBTB, GO and three

representative nanocomposites were exposed to the environment under 99% RH at 30 °C for 2 days, immediately followed by the TGA measurement of each sample in order to quantify their water uptakes from the humid environment.[29, 34] The obtained TGA data are shown in Figure 7(a). The weight loss of each sample before the plateau at 110 °C, a temperature slightly higher than the boiling point of water, indicates the amount of physically adsorbed water in the material.[29] The resulting water uptakes are plotted in Figure 7(b). It can be seen that the trend in TGA results is exactly consistent with that in the proton-conducting performance, with ZrBTB/0.005GO exhibiting the highest σ value and ZrBTB–0.01GO showing the lowest σ value. The E_a values, derived from Arrhenius plots, also have the same trend, with ZrBTB/0.005GO possessing the smallest E_a and ZrBTB–0.01GO having the largest E_a. Findings here indicate that for these materials, the amount of water in the hydrogen-bonding network governs the Grotthuss-type proton transport. With a small amount of GO, *i.e.*, around 1 wt% or 0.5 wt% here, to form composites with ZrBTB, it creates more voids between flower-like aggregates of ZrBTB sheets and turns the morphology of the material into loosely packed tiny 2D sheets (see Figure 3); such morphologies should provide more locations to capture and accumulate water molecules. However, for ZrBTB–0.01GO, its chemical coordination between GO and MOF reduces the amounts of accessible hydrophilic functional groups on both materials, leading to a reduced water uptake. With the physically blended nanocomposites, more voids between aggregates of MOF sheets are presented compared to the pristine ZrBTB, with hydrophilic groups from both ZrBTB and GO well-preserved. They can thus adsorb more water molecules from the humid air under a high RH, which is the cause for their better proton-conducting performance compared to those of both the pristine ZrBTB and pristine GO.

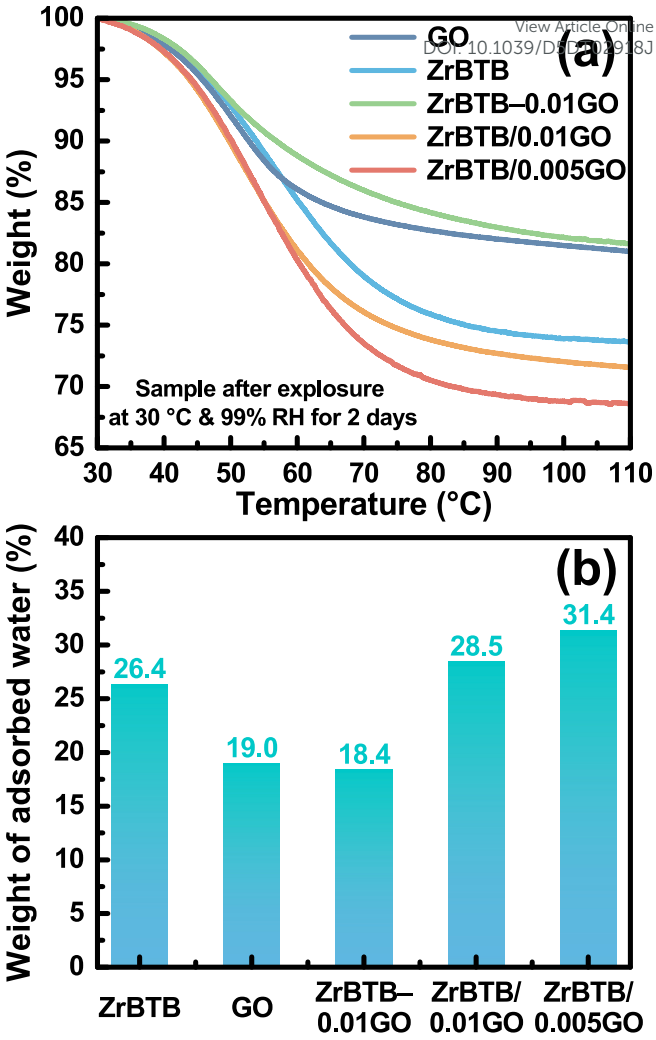

Figure 7. (a) TGA curves of various materials, after 2 days of exposure to the environment under 99% RH at 30 °C. Ramping rate: 1 degree/min. (b) Mass fraction of adsorbed water in each material prior to the TGA measurement, extracted from data shown in (a).

Conclusions

ZrBTB and their nanocomposites with GO were successfully synthesised by performing either chemical grafting or physical blending, enabling a systematic investigation on their proton-conducting behaviours. Nanocomposites synthesised by both methods possess a similar morphology, with aggregates of loosely packed small 2D sheets. However, the coordination between GO and ZrBTB through carboxylate groups can be found in the chemically grafted nanocomposite, as evidenced by FTIR data. All MOF-based materials can preserve their crystallinity and coordination characteristics after the pelletising process and EIS measurements under 99% RH. The chemically grafted nanocomposite shows worse proton-conducting performance compared to pristine materials. On the other hand, the physically blended composites can outperform both pristine materials as proton conductors, with ZrBTB/0.005GO achieving an ultrahigh σ of 1.03×10^{-1} S cm^{-1}

at 60 °C under 99% RH and a relatively small E_a of 0.18 eV. This superior performance is attributed to the cooperative effect of hydrophilic functional groups from GO and the hydroxyl groups on nodes of ZrBTB, which enhance the water uptake and promote the formation of a continuous hydrogen-bonding network. As the first study reporting proton-conducting behaviours in composites composed of 2D MOF and GO, findings here suggest that for 2D MOF-based materials, physical blending is a simpler and more effective strategy to synthesise nanocomposites than chemical grafting, aiming to develop high-performance proton-conductive materials.

Conflicts of interest

There are no conflicts to declare.

Acknowledgements

This work is financially supported by National Science and Technology Council (NSTC) of Taiwan, under the following grants: 112-2223-E-006-003-MY3 and 113-2923-E-006-006-MY2. This study is also in part funded by Ministry of Education (MOE) of Taiwan, under Yushan Young Fellow Program (MOE-112-YSFEE-0005-001-P2) and Higher Education Sprout Project under National Cheng Kung University (NCKU). We also thank Core Facility Center of NCKU for conducting both TEM measurements and TGA analyses.

References

1. H. Furukawa, K. E. Cordova, M. O'Keeffe and O. M. Yaghi, *Science*, 2013, **341**, 1230444.
2. S. Kitagawa, R. Kitaura and S. i. Noro, *Angew. Chem. Int. Ed.*, 2004, **43**, 2334-2375.
3. L. J. Murray, M. Dincă and J. R. Long, *Chem. Soc. Rev.*, 2009, **38**, 1294-1314.
4. J. L. Obeso, V. B. López-Cervantes, C. V. Flores, A. Martínez, Y. A. Amador-Sánchez, N. S. Portillo-Velez, H. A. Lara-García, C. Leyva, D. Solis-Ibarra and R. A. Peralta, *Dalton Trans.*, 2024, **53**, 4790-4796.
5. J.-R. Li, J. Sculley and H.-C. Zhou, *Chem. Rev.*, 2012, **112**, 869-932.
6. T. Chen and D. Zhao, *Coord. Chem. Rev.*, 2023, **491**, 215259.
7. Y. Liu, A. J. Howarth, J. T. Hupp and O. K. Farha, *Angew. Chem. Int. Ed.*, 2015, **54**, 9001-9005.
8. S. H. Park, H. M. Kim, M. L. Díaz-Ramírez, S. Lee and N. C. Jeong, *Chem. Commun.*, 2024, **60**, 14577-14580.
9. L. E. Kreno, K. Leong, O. K. Farha, M. Allendorf, R. P. Van Duyne and J. T. Hupp, *Chem. Rev.*, 2012, **112**, 1105-1125.
10. M. Ko, L. Mendecki, A. M. Eagleton, C. G. Durbin, R. M. Stolz, Z. Meng and K. A. Mirica, *J. Am. Chem. Soc.*, 2020, **142**, 11717-11733.
11. D. Sheberla, J. C. Bachman, J. S. Elias, C.-J. Sun, Y. Shao-Horn and M. Dincă, *Nat. Mater.*, 2016, **16**, 220-224.
12. G. Lee, G. Park and S. S. Park, *J. Am. Chem. Soc.*, 2024, **146**, 29767-29772.
13. S. Bureekaew, S. Horike, M. Higuchi, M. Mizuno, T. Kawamura, D. Tanaka, N. Yanai and S. Kitagawa, *Nat. Mater.*, 2009, **8**, 831-836.
14. T. Yamada, K. Otsubo, R. Makiura and H. Kitagawa, *Chem. Soc. Rev.*, 2013, **42**, 6655-6669.
15. P. Ramaswamy, N. E. Wong and G. K. Shimizu, *Chem. Soc. Rev.*, 2014, **43**, 5913-5932.
16. W. J. Phang, H. Jo, W. R. Lee, J. H. Song, K. Yoo, B. Kim and C. S. Hong, *Angew. Chem. Int. Ed.*, 2015, **54**, 5142-5146.
17. K. i. Otake and H. Kitagawa, *Small*, 2021, **17**, 2006189.
18. K.-P. Chen, Y. Ma, H.-X. Ren, C.-X. Zhang and Q.-L. Wang, *Dalton Trans.*, 2024, **53**, 8716-8721.
19. K.-X. Zhao, G.-Q. Zhang, X.-R. Wu, H.-B. Luo, Z.-X. Han, Y. Liu and X.-M. Ren, *ACS Appl. Electron. Mater.*, 2025, **7**, 3164-3175.
20. S. Biswas, D. K. Thapa and L. Mandal, *Dalton Trans.*, 2025, **54**, 1750-1769.
21. K. Jiao, J. Xuan, Q. Du, Z. Bao, B. Xie, B. Wang, Y. Zhao, L. Fan, H. Wang and Z. Hou, *Nature*, 2021, **595**, 361-369.
22. Y. Wang, D. F. R. Diaz, K. S. Chen, Z. Wang and X. C. Adroher, *Mater. Today*, 2020, **32**, 178-203.
23. A. J. Howarth, Y. Liu, P. Li, Z. Li, T. C. Wang, J. T. Hupp and O. K. Farha, *Nat. Rev. Mater.*, 2016, **1**, 1-15.
24. S. Yuan, J.-S. Qin, C. T. Lollar and H.-C. Zhou, *ACS Cent. Sci.*, 2018, **4**, 440-450.
25. M.-D. Tsai, K.-C. Wu and C.-W. Kung, *Chem. Commun.*, 2024, **60**, 8360-8374.
26. C.-H. Wu, K.-C. Wu, C.-H. Shen and C.-W. Kung, *Coord. Chem. Rev.*, 2025, **538**, 216704.
27. X. Chen and G. Li, *Inorg. Chem. Front.*, 2020, **7**, 3765-3784.
28. G. K. Shimizu, J. M. Taylor and S. Kim, *Science*, 2013, **341**, 354-355.
29. W. H. Ho, S.-C. Li, Y.-C. Wang, T.-E. Chang, Y.-T. Chiang, Y.-P. Li and C.-W. Kung, *ACS Appl. Mater. Interfaces*, 2021, **13**, 55358-55366.
30. M. Szufla, A. Choroś, W. Nitek and D. Matoga, *Chem. Eur. J.*, 2022, **28**, e202200835.
31. M. Szufla, J. A. R. Navarro, K. Góra-Marek and D. Matoga, *ACS Appl. Mater. Interfaces*, 2023, **15**, 28184-28192.
32. M. K. Sarango-Ramírez, M. Donoshita, Y. Yoshida, D. W. Lim and H. Kitagawa, *Angew. Chem. Int. Ed.*, 2023, **62**, e202301284.
33. Y. Zheng, Y. Liu, H. Li, Z. Yang, W. Wu, J. Zhang, J. Wu and J. Wang, *Adv. Funct. Mater.*, 2025, **35**, 2500151.
34. F. Yang, H. Huang, X. Wang, F. Li, Y. Gong, C. Zhong and J.-R. Li, *Cryst. Growth Des.*, 2015, **15**, 5827-5833.
35. S.-L. Zheng, C.-M. Wu, L.-H. Chung, H.-Q. Zhou, J. Hu, Z. Liu, Y. Wu, L. Yu and J. He, *ACS Energy Lett.*, 2023, **8**, 3095-3101.
36. L. Yang, B. Tang and P. Wu, *J. Mater. Chem. A*, 2015, **3**, 15838-15842.
37. Z. Rao, K. Feng, B. Tang and P. Wu, *J. Membr. Sci.*, 2017, **533**, 160-170.
38. P. M. Unnikrishnan, G. Premanand and S. K. Das, *Inorg. Chem.*, 2025, **64**, 3506-3517.
39. M. R. Karim, K. Hatakeyama, T. Matsui, H. Takehira, T. Taniguchi, M. Koinuma, Y. Matsumoto, T. Akutagawa, T. Nakamura, S.-i. Noro, T. Yamada, H. Kitagawa and S. Hayami, *J. Am. Chem. Soc.*, 2013, **135**, 8097-8100.
40. L. Glasser, *Chem. Rev.*, 1975, **75**, 21-65.
41. K. D. Kreuer, A. Rabenau and W. Weppner, *Angew. Chem. Int. Ed. Engl.*, 1982, **21**, 208-209.

Dalton Transactions ARTICLE

View Article Online
DOI: 10.1039/D5DT02918J

42. I. S. Kim, J. Borycz, A. E. Platero-Prats, S. Tussupbayev, T. C. Wang, O. K. Farha, J. T. Hupp, L. Gagliardi, K. W. Chapman, C. J. Cramer and A. B. F. Martinson, *Chem. Mater.*, 2015, **27**, 4772-4778.
43. Z. Hu, E. M. Mahdi, Y. Peng, Y. Qian, B. Zhang, N. Yan, D. Yuan, J.-C. Tan and D. Zhao, *J. Mater. Chem. A*, 2017, **5**, 8954-8963.
44. L. Feng, Y. Qiu, Q.-H. Guo, Z. Chen, J. S. W. Seale, K. He, H. Wu, Y. Feng, O. K. Farha, R. D. Astumian and J. F. Stoddart, *Science*, 2021, **374**, 1215-1221.
45. Y.-L. Chen, C.-H. Shen, C.-W. Huang and C.-W. Kung, *Mol. Syst. Des. Eng.*, 2023, **8**, 330-340.
46. T.-C. Lin, K.-C. Wu, J.-W. Chang, Y.-L. Chen, M.-D. Tsai and C.-W. Kung, *Dalton Trans.*, 2024, **53**, 11426-11435.
47. K.-C. Wu, M.-D. Tsai, C.-H. Wu, T.-H. Yang, Y.-L. Chen and C.-W. Kung, *APL Mater.*, 2024, **12**.
48. J.-W. Chang, T.-C. Lin, Y.-L. Chen, P.-C. Han, S.-C. Yang, M.-D. Tsai, K. C. W. Wu and C.-W. Kung, *CrystEngComm*, 2024, **26**, 2852-2861.
49. L. Stobinski, B. Lesiak, A. Malolepszy, M. Mazurkiewicz, B. Mierzwa, J. Zemek, P. Jiricek and I. Bieloshapka, *J. Electron Spectrosc. Relat. Phenom.*, 2014, **195**, 145-154.
50. M.-D. Tsai, Y.-L. Chen, J.-W. Chang, S.-C. Yang and C.-W. Kung, *ACS Appl. Energy Mater.*, 2023, **6**, 11268-11277.
51. R. Shimoni, Z. Shi, S. Binyamin, Y. Yang, I. Liberman, R. Ifraemov, S. Mukhopadhyay, L. Zhang and I. Hod, *Angew. Chem. Int. Ed.*, 2022, **61**, e202206085.
52. Y. Li and R. T. Yang, *Langmuir*, 2007, **23**, 12937-12944.
53. S. Ullah, M. A. Bustam, M. A. Assiri, A. G. Al-Sehemi, G. Gonfa, A. Mukhtar, F. A. Abdul Kareem, M. Ayoub, S. Saqib and N. B. Mellon, *Microporous Mesoporous Mater.*, 2020, **294**, 109844.
54. S. Thakur and N. Karak, *Carbon*, 2012, **50**, 5331-5339.
55. G. Srinivas, J. W. Burress, J. Ford and T. Yildirim, *J. Mater. Chem.*, 2011, **21**, 11323-11329.
56. V. Brusko, A. Khannanov, A. Rakhmatullin and A. M. Dimiev, *Carbon*, 2024, **229**, 119507.
57. R. Al-Gaashani, A. Najjar, Y. Zakaria, S. Mansour and M. A. Atieh, *Ceram. Int.*, 2019, **45**, 14439-14448.
58. L. Liu, Z. Qiao, X. Cui, C. Pang, H. Liang, P. Xie, X. Luo, Z. Huang, Y. Zhang and Z. Zhao, *ACS Appl. Mater. Interfaces*, 2019, **11**, 23039-23049.
59. C.-H. Shen, Y. Zhao, H. N. Nam, L. Zhu, Q. M. Phung, V. Austen, M. Kim, D. Jiang, X. Wei, T. Yokoshima, C.-W. Kung and Y. Yamauchi, *Chem. Sci.*, 2025, **16**, 7026-7038.
60. T. Shen, X. Feng, L. Fan, L. Li, Y. Zhang, B. Chai, U. Khan and X. Wang, *Cryst. Growth Des.*, 2025, **25**, 5312-5320.
61. J. Liu, Z. Li, X. Zhang, K.-i. Otake, L. Zhang, A. W. Peters, M. J. Young, N. M. Bedford, S. P. Letourneau, D. J. Mandia, J. W. Elam, O. K. Farha and J. T. Hupp, *ACS Catal.*, 2019, **9**, 3198-3207.
62. A. R. Heiba, M. O. Abdel-Salam, T. Yoon and E. El Sawy, *Nanoscale*, 2025, **17**, 459-473.
63. T. E. DeCoursey and V. V. Cherny, *J. Gen. Physiol.*, 1997, **109**, 415-434.
64. D. W. Kang, K. S. Lim, K. J. Lee, J. H. Lee, W. R. Lee, J. H. Song, K. H. Yeom, J. Y. Kim and C. S. Hong, *Angew. Chem. Int. Ed.*, 2016, **55**, 16123-16126.
65. F. Yang, G. Xu, Y. Dou, B. Wang, H. Zhang, H. Wu, W. Zhou, J.-R. Li and B. Chen, *Nat. Energy*, 2017, **2**, 877-883.

All data supporting this article have been included in the manuscript or included as part of the Supplementary Information.

View Article Online
DOI: 10.1039/D5DT02918J